

3D Feature Estimation for Sparse, Nonlinear Bistatic SAR Apertures

Julie Ann Jackson

Dept. of Electrical and Computer Engineering
Air Force Institute of Technology
Dayton, Ohio, 45433
Email: julie.jackson@afit.edu

Randolph L. Moses

Dept. of Electrical and Computer Engineering
The Ohio State University
Columbus, Ohio, 43210
Email: moses.2@osu.edu

Abstract—We present an algorithm for extracting 3D canonical scattering features observed over sparse, bistatic SAR apertures. The input to the algorithm is a collection of noisy bistatic measurements which are, in general, collected over nonlinear flight paths. The output of the algorithm is a set of canonical scattering features that describe the 3D scene geometry. The algorithm employs a pragmatic approach to initializing feature estimates by first forming a 3D reflectivity reconstruction using sparsity-regularized least squares methods. Regions of high energy are detected in the reconstructions to obtain initial feature estimates. A single canonical feature, corresponding to a geometric shape primitive, is fit to each region via nonlinear optimization of fit error between the complex phase history data and parametric scattering models using a modification of the CLEAN method. Feature extraction results are presented for sparsely-sampled, nonlinear, 3D bistatic scattering prediction data of a simple scene.

Index Terms—synthetic aperture radar, bistatic scattering, feature extraction, radar target recognition

I. INTRODUCTION

We propose an algorithm for extracting attributed 3D features from SAR data collected over sparse, nonlinear apertures that have frequency, azimuth, and elevation diversity. Practical SAR flight paths provide only a sparse sampling of a 3D SAR aperture, resulting in high sidelobes and aliasing if traditional backprojection or Fourier imaging is used. Recent application of regularization techniques has shown promise in removing these image artifacts to obtain high quality 3D images with regions of compact energy [1]–[3]. We propose a feature extraction algorithm that uses the regularization approach to generate such sparse 3D images for detection of scatterers and initialization of feature parameter estimates. The algorithm processes fully-polarimetric phase history data and outputs a list of scattering primitives, characterized by their type, location, orientation, and size. We present the algorithm for the general case of bistatic SAR apertures, but it is also applicable to monostatic SAR, as a special case of the bistatic geometry.

In Section II we present parametric scattering models for canonical features of interest. In Section III we discuss the

feature extraction problem and outline an algorithm for extracting features from polarimetric phase history data. In Section V we apply the algorithm to simulated data for an arbitrary, nonlinear, sparse bistatic SAR aperture.

II. BISTATIC CANONICAL SCATTERING MODELS

We assume that scattering from an object can be represented as a sum of responses from canonical scattering centers. A set of 3D canonical models have recently been developed for bistatic measurements [4], [5]. These models include a plate, dihedral, trihedral, top-hat, cylinder, and sphere. In this section we briefly review the models; details on their derivations are found in [4], [5].

Using high-frequency approximations [6], we represent the received radar signal $S(k, \mathbf{\Lambda}; \mathbf{\Theta}; \mathbf{\Gamma})$ as a sum of scatterers $S_q(k, \mathbf{\Lambda}; \mathbf{\Theta}_q, \mathbf{\Gamma}_q)$. The sum may be written as

$$S(k, \mathbf{\Lambda}; \mathbf{\Theta}; \mathbf{\Gamma}) = \sum_{q=1}^Q P_{\beta_q}(\mathbf{\Lambda}; \mathbf{\Theta}_q) M_{\Gamma_q}(k, \mathbf{\Lambda}; \mathbf{\Theta}_q) e^{jk\Delta R(\mathbf{\Lambda}; \mathbf{\Theta}_q)} \quad (1)$$

where $k \triangleq \frac{2\pi f}{c}$ is the wavenumber for frequency f and speed of light c . We use the shorthand notation $\mathbf{\Lambda} = (\phi_t, \theta_t, \phi_r, \theta_r)$ to represent the scattered signal dependence on the transmitter (subscript t) and receiver (subscript r) azimuth (ϕ) and elevation (θ) locations. The term P_{β_q} is the 2×2 polarization scattering matrix of the q th scatterer, which takes the form

$$P_{\beta_q=\text{odd}}(\mathbf{\Lambda}; \mathbf{\Theta}_q) = \begin{bmatrix} -1 & 0 \\ 0 & -1 \end{bmatrix} \quad (2)$$

for *odd*-bounce scatterers or

$$P_{\beta_q=\text{even}}(\mathbf{\Lambda}; \mathbf{\Theta}_q) = \begin{bmatrix} -\cos(\zeta_t + \zeta_r) & \sin(\zeta_t + \zeta_r) \\ \sin(\zeta_t + \zeta_r) & \cos(\zeta_t + \zeta_r) \end{bmatrix} \quad (3)$$

for *even*-bounce scatterers, where ζ_t and ζ_r are the object rotation angles about the transmitter and receiver antenna lines of sight (LOS). The subscript $\mathbf{\Gamma}_q$ in (1) indicates the type of scatterer (plate, dihedral, etc.) and encodes the particular functional form of the amplitude response M_{Γ_q} . The vector $\mathbf{\Theta}_q$ contains physical parameters corresponding to a reflector of type $\mathbf{\Gamma}_q$, including (x, y, z) location, roll ($\tilde{\gamma}$), pitch ($\tilde{\theta}$), yaw ($\tilde{\phi}$) orientation, and length, height, and/or radius size parameters, as applicable. Finally, the term ΔR in (1) is the

This work was performed while J. Jackson was a Graduate fellow at OSU, with funding from OSU and the Dayton Area Graduate Studies Institute. The views expressed in this article are those of the authors and do not reflect the official policy or position of the United States Air Force, Department of Defense, or the U.S. Government. Approved for public release: #091064.

Report Documentation Page			Form Approved OMB No. 0704-0188		
Public reporting burden for the collection of information is estimated to average 1 hour per response, including the time for reviewing instructions, searching existing data sources, gathering and maintaining the data needed, and completing and reviewing the collection of information. Send comments regarding this burden estimate or any other aspect of this collection of information, including suggestions for reducing this burden, to Washington Headquarters Services, Directorate for Information Operations and Reports, 1215 Jefferson Davis Highway, Suite 1204, Arlington VA 22202-4302. Respondents should be aware that notwithstanding any other provision of law, no person shall be subject to a penalty for failing to comply with a collection of information if it does not display a currently valid OMB control number.					
1. REPORT DATE MAY 2010		2. REPORT TYPE		3. DATES COVERED 00-00-2010 to 00-00-2010	
4. TITLE AND SUBTITLE 3D Feature Estimation for Sparse, Nonlinear Bistatic SAR Apertures				5a. CONTRACT NUMBER	
				5b. GRANT NUMBER	
				5c. PROGRAM ELEMENT NUMBER	
6. AUTHOR(S)				5d. PROJECT NUMBER	
				5e. TASK NUMBER	
				5f. WORK UNIT NUMBER	
7. PERFORMING ORGANIZATION NAME(S) AND ADDRESS(ES) Air Force Institute of Technology, Dept. of Electrical and Computer Engineering, Dayton, OH, 45433				8. PERFORMING ORGANIZATION REPORT NUMBER	
9. SPONSORING/MONITORING AGENCY NAME(S) AND ADDRESS(ES)				10. SPONSOR/MONITOR'S ACRONYM(S)	
				11. SPONSOR/MONITOR'S REPORT NUMBER(S)	
12. DISTRIBUTION/AVAILABILITY STATEMENT Approved for public release; distribution unlimited					
13. SUPPLEMENTARY NOTES See also ADM002322. Presented at the 2010 IEEE International Radar Conference (9th) Held in Arlington, Virginia on 10-14 May 2010. Sponsored in part by the Navy.					
14. ABSTRACT We present an algorithm for extracting 3D canonical scattering features observed over sparse, bistatic SAR apertures. The input to the algorithm is a collection of noisy bistatic measurements which are, in general, collected over nonlinear flight paths. The output of the algorithm is a set of canonical scattering features that describe the 3D scene geometry. The algorithm employs a pragmatic approach to initializing feature estimates by first forming a 3D reflectivity reconstruction using sparsityregularized least squares methods. Regions of high energy are detected in the reconstructions to obtain initial feature estimates. A single canonical feature, corresponding to a geometric shape primitive, is fit to each region via nonlinear optimization of fit error between the complex phase history data and parametric scattering models using a modification of the CLEAN method. Feature extraction results are presented for sparsely-sampled nonlinear, 3D bistatic scattering prediction data of a simple scene.					
15. SUBJECT TERMS					
16. SECURITY CLASSIFICATION OF:			17. LIMITATION OF ABSTRACT Same as Report (SAR)	18. NUMBER OF PAGES 6	19a. NAME OF RESPONSIBLE PERSON
a. REPORT unclassified	b. ABSTRACT unclassified	c. THIS PAGE unclassified			

bistatic differential range, which may be approximated under a far-field assumption as

$$\Delta R(\mathbf{\Lambda}; \mathbf{\Theta}_q) = \Delta R_r(\mathbf{\Lambda}; \mathbf{\Theta}_q) + x_q(\cos \phi_t \cos \theta_t + \cos \phi_r \cos \theta_r) + y_q(\sin \phi_t \cos \theta_t + \sin \phi_r \cos \theta_r) + z_q(\sin \theta_t + \sin \theta_r) \quad (4)$$

where (x_q, y_q, z_q) is the center location of the scatterer and $\Delta R_r(\mathbf{\Lambda}; \mathbf{\Theta}_q)$ is a range offset term due to the distance of the scatterer surface from the scatterer center location.

Table I lists canonical shape bistatic scattering models as functions of relative aspect angles (ϕ'_t, θ'_t) and (ϕ'_r, θ'_r) that encode both the radar antenna aspect angles and the object's roll, pitch, and yaw orientation. (See the model derivations in [4], [5] for details on computing the relative aspect angles). Table I also lists a calibration scale factor A_{cal} , which when substituted in place of the scalar amplitude term A in M_Γ , scales the peak scattering intensity $\max(|S_{\Gamma_q}|^2)$ to equal the peak radar cross section (RCS) of the object.

Substituting the model terms from Table I into (1) we obtain a description of the scattering response of a set of reflectors as a function of the data collection parameters (radar antenna locations and frequency) and object parameters (shape type, location, size, and orientation). We assume that the radar antenna parameters are known and that the object parameters are unknown. In the sequel, we consider estimating the object parameters to obtain a physical description of target structure.

III. FEATURE EXTRACTION

Using the models in Section II, we consider the problem of extracting scattering features from a set of noisy bistatic phase history measurements, $\mathbf{Y}(k, \mathbf{\Lambda})$. Under the assumption of white Gaussian measurement noise, maximum likelihood parameter estimates of the scattering parameters can be found by solving the least squares (LS) problem:

$$\min_{\mathbf{\Theta}, \mathbf{\Gamma}} \left\| \mathbf{Y}(k, \mathbf{\Lambda}) - \sum_{n=1}^N \mathbf{S}_n(k, \mathbf{\Lambda}; \mathbf{\Theta}_n, \mathbf{\Gamma}_n) \right\|_2^2. \quad (5)$$

Note that (5) is a combined detection and estimation problem. The detection problem is to determine the scattering types $\mathbf{\Gamma} = [\mathbf{\Gamma}_1, \dots, \mathbf{\Gamma}_N]$, and the estimation problem is to solve for the parameter vector $\mathbf{\Theta} = [\mathbf{\Theta}_1, \dots, \mathbf{\Theta}_N]$ that characterizes the location, orientation, and sizes of the scattering features. In addition, there is a model order selection problem of choosing N in (5); ideally $N = Q$, the true model order in (1).

For the models in Section II, (5) is a high order, nonlinear, non-convex optimization problem that requires accurate initialization for iterative numerical solvers to converge to the global minimum. Previous work utilizes energy compactness in 2D SAR images to initialize model order and scatterer location and size parameters [7], [8]. However, 3D SAR flight paths are often sparse apertures, and the corresponding Fourier-based or backprojection-formed images contain high sidelobes and aliasing, hindering feature segmentation in the image domain. For example, Figure 2(a) shows the phase history for an arbitrary sparse bistatic aperture, and Figure 2(b) shows the

corresponding Fourier image. From the image, it is difficult to discern the number and locations of the scatterers.

Recent application of regularization techniques [1], [2] has demonstrated effective formation of high-quality sparse 3D images [3]. Therefore, we propose a pragmatic 3D feature extraction algorithm that first generates sparse 3D images using ℓ_1 -Regularized Least Squares. These sparse images are used to initialize model order and scatterer location, orientation, and size parameter estimates. Parameter estimates are refined for one scatterer at a time using a modification of CLEAN [9]. The algorithm output is a list of detected features and the corresponding model parameter estimates. Key steps of the proposed feature extraction algorithm are summarized below.

A. 3D Sparse Image Formation

Let the underlying scene reflectivity (sparse image) be given by \mathbf{s} and let Φ be a mapping of the reflectivity to the observed phase history at the observed transmit and receive angles $\mathbf{\Lambda}$. Then, the ℓ_1 -regularized least squares problem

$$\hat{\mathbf{s}} = \arg \min_{\mathbf{s}} \|\mathbf{Y} - \Phi \mathbf{s}\|_2^2 + \lambda \|\mathbf{s}\|_1 \quad (6)$$

may be solved to obtain a sparse image solution $\hat{\mathbf{s}}$ with sparsity enforced by the scalar constraint λ . For our SAR imaging problem, the mapping Φ is given by $H F^H$, where F is a discrete Fourier transform matrix, H is a projection of the phase history onto the flight path samples, and superscript H is the matrix Hermitian operator. We follow [1], [2] to efficiently compute the ℓ_1 -regularized sparse image $\hat{\mathbf{s}}$. A sparse solution that is jointly optimal across all polarizations is preferred, but for computational reasons we independently compute sparse images for each polarization channel and denote the solutions as $\hat{\mathbf{s}}_p, p \in \{\text{HH}, \text{HV}, \text{VH}, \text{VV}\}$. We form a composite image

$$\hat{\mathbf{s}}_c = [|\hat{\mathbf{s}}_{\text{HH}}|^2 + |\hat{\mathbf{s}}_{\text{HV}}|^2 + |\hat{\mathbf{s}}_{\text{VH}}|^2 + |\hat{\mathbf{s}}_{\text{VV}}|^2]^{1/2} \quad (7)$$

from the images corresponding to the four polarization channels. An example sparse image is shown in Figure 3. We assume each region of high energy in the composite image $\hat{\mathbf{s}}_c$ corresponds to one scatterer and use the image to initialize the scatterer location, orientation, and size parameters.

B. Image Segmentation

We extend the Peak Region Segmentation algorithm in [10] to segment three-dimensional SAR images. We implement a region merging method that accounts for noise ripple across extended radar targets but still separates closely-spaced scatterers. Details are found in [11]. Figure 4 shows that application of this automated segmentation algorithm to the sparse image in Figure 3 results in seven distinct scattering regions.

C. Parameter Initialization

We assume that each segmented image region corresponds to one scatterer. Therefore, we initialize scatterer location estimates for the plate, dihedral, and trihedral shapes at the centroid of the image segment of interest. For the cylinder, top-hat, and sphere, the location of energy in the image is offset from the scatterer location by the shape's non-zero radius. For

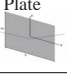



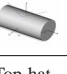

Shape Type Γ	Bounce Type β	Amplitude Response $M_\Gamma(k, \mathbf{\Lambda}; \Theta)$	Calibration A_{cal}	Range Offset ΔR_r
	odd	$\frac{jk}{\sqrt{\pi}} A \text{sinc}\left[k \frac{H}{2} (\sin \theta'_t + \sin \theta'_r)\right] \text{sinc}\left[k \frac{L}{2} (\sin \phi'_t \cos \theta'_t + \sin \phi'_r \cos \theta'_r)\right]$ $\phi'_t, \phi'_r \in [-\frac{\pi}{2}, \frac{\pi}{2}], \theta'_t, \theta'_r \in [-\frac{\pi}{2}, \frac{\pi}{2}]$	LH	0
	even	$\frac{jk}{\sqrt{\pi}} A \text{sinc}\left[kH (\cos \theta'_t - \cos \theta'_r)\right] \text{sinc}\left[k \frac{L}{2} (\sin \phi'_t \cos \theta'_t + \sin \phi'_r \cos \theta'_r)\right]$ $\times \begin{cases} \sin\left(\frac{\theta'_t + \theta'_r}{2}\right), & \theta'_t, \theta'_r \in [0, \frac{\pi}{4}] \\ \cos\left(\frac{\theta'_t + \theta'_r}{2}\right), & \theta'_t, \theta'_r \in [\frac{\pi}{4}, \frac{\pi}{2}] \end{cases}, \phi'_t, \phi'_r \in [-\frac{\pi}{2}, \frac{\pi}{2}]$	$2LH$	0
	odd	$\frac{jk}{2\sqrt{\pi}} A \text{sinc}\left[kH (\cos \theta'_t - \cos \theta'_r)\right] \left[\text{sinc}\left[kH (\cos(\phi'_r - \frac{\pi}{4}) \cos \theta'_r - \cos(\phi'_t - \frac{\pi}{4}) \cos \theta'_t)\right] \right.$ $\left. + \text{sinc}\left[kH (\cos(\phi'_r + \frac{\pi}{4}) \cos \theta'_r - \cos(\phi'_t + \frac{\pi}{4}) \cos \theta'_t)\right] \right]$ $\times \begin{cases} \sin\left(\frac{\theta'_t + \theta'_r}{2} + \frac{\pi}{4} - \tan^{-1}\left(\frac{1}{\sqrt{2}}\right)\right), & \theta'_r \in [0, \tan^{-1}\left(\frac{1}{\sqrt{2}}\right)] \\ \cos\left(\frac{\theta'_t + \theta'_r}{2} + \frac{\pi}{4} - \tan^{-1}\left(\frac{1}{\sqrt{2}}\right)\right), & \theta'_r \in [\tan^{-1}\left(\frac{1}{\sqrt{2}}\right), \frac{\pi}{2}] \end{cases} \begin{cases} -\cos\left(\frac{\phi'_t + \phi'_r}{2} - \frac{\pi}{4}\right), & \phi'_r \in [-\frac{\pi}{4}, 0] \\ \sin\left(\frac{\phi'_t + \phi'_r}{2} - \frac{\pi}{4}\right), & \phi'_r \in [0, \frac{\pi}{4}] \end{cases}$	$2\sqrt{3}H^2$	0
	odd	$\sqrt{\frac{jk}{\cos \phi'_t}} A \cos \phi'_r \text{sinc}\left[k \frac{L}{2} (\sin \phi'_t \cos \theta'_t + \sin \phi'_r \cos \theta'_r)\right], \phi'_t, \phi'_r \in [-\frac{\pi}{2}, \frac{\pi}{2}]$	$L\sqrt{r}$	$r \cos\left(\frac{\theta'_t - \theta'_r}{2}\right) (\cos \phi'_t + \cos \phi'_r)$
	even	$A\sqrt{jk} \text{sinc}\left[kH (\cos \theta'_t - \cos \theta'_r)\right] \times \begin{cases} \sin\left(\frac{\theta'_t + \theta'_r}{2}\right), & \theta'_t, \theta'_r \in [0, \frac{\pi}{4}] \\ \cos\left(\frac{\theta'_t + \theta'_r}{2}\right), & \theta'_t, \theta'_r \in [\frac{\pi}{4}, \frac{\pi}{2}] \end{cases}$	$\sqrt{\frac{8r}{\sqrt{2}}} H$	$r \cos\left(\frac{\phi'_t - \phi'_r}{2}\right) (\cos \theta'_t + \cos \theta'_r)$
	odd	$A\sqrt{\pi}$	1	$r (\cos \theta'_t + \cos \theta'_r) \cos\left(\frac{\phi'_t - \phi'_r}{2}\right) \cos\left(\frac{\theta'_t + \theta'_r}{2}\right) + r \sin\left(\frac{\theta'_t + \theta'_r}{2}\right) (\sin \theta'_t + \sin \theta'_r)$

TABLE I
PARAMETRIC BISTATIC SCATTERING MODELS FROM [4], [5].

these shapes, we test multiple scattering locations near the image segment centroid to obtain low-cost initialization points for numerical estimation of the object location and radius. Length and height parameters are initialized for all shapes by computing the extent of the segmented image regions. Scatterer orientation is initially estimated by computing the rotations between the image coordinate axes and the principal scattering directions of each segmented image region. For details of the parameter initialization scheme, see [11].

D. Feature Shape Classification

The image segmentation and parameter initialization schemes provide information about the location, spread, and orientation of the scattered energy in the scene, but they do not identify the canonical shape type associated with each region. We implement four shape discrimination methods that test the data polarization response, model fit, predicted radar cross section, and predicted object size.

1) *Polarization*: We use the polarization response from the sparse images obtained from (6) to classify observed features as odd-bounce or even-bounce scatterers. We extend the polarimetric classification scheme in [8] to define odd-bounce and even-bounce scattering basis vectors for the bistatic case as

$$B_{\text{odd}} = \begin{bmatrix} 1 \\ 0 \\ 0 \end{bmatrix} \quad B_{\text{even}} = \begin{bmatrix} 0 \\ \cos(\zeta_t + \zeta_r) \\ \sin(\zeta_t + \zeta_r) \end{bmatrix} \quad (8)$$

for LOS rotation angles ζ_t and ζ_r [11].

The bounce type of the i th voxel in the SAR image is estimated by finding the least-squares distance between the

basis vectors B in (8) and the polarimetric scattering response vector $\bar{\mathbf{s}}_i = [\mathbf{s}_{\text{HH}_i}, \frac{1}{2}(\mathbf{s}_{\text{HV}_i} + \mathbf{s}_{\text{VH}_i}), \mathbf{s}_{\text{VV}_i}]^T$. Formally,

$$\text{bounce}_i = \arg \min_{\substack{\psi, \\ \beta \in \{\text{odd}, \text{even}\}}} \left\| \bar{\mathbf{s}}_i - B_\beta^T \bar{\mathbf{s}}_i \begin{bmatrix} \frac{1}{\sqrt{2}} & \frac{1}{\sqrt{2}} & 0 \\ 0 & 0 & 1 \\ \frac{1}{\sqrt{2}} & \frac{-1}{\sqrt{2}} & 0 \end{bmatrix} B_\beta \right\|. \quad (9)$$

The example in Figure 5 shows polarization bounce type estimates for the image segments in Figure 4 that correspond to the correct bounce types. Thus, we use choose the subset of canonical shapes with the estimated bounce type as the candidate scatterer types for each image segment.

2) *Model Fit*: The six scattering models in Table I have similar functional forms, and confusion between models may arise when estimating the best model fit to the data. Therefore, we fit to the data the $j = 1, \dots, J$ candidate models whose polarization matches that determined by the polarization classification in (9) and make a list \hat{F} of best-fit models Γ_j as

$$\hat{F} = \arg \left\{ \left(\epsilon_{\Gamma_j} - \min_{\Gamma_j} \epsilon_{\Gamma_j} \right) < \tau_{\text{fit}} \right\} \quad (10)$$

where ϵ_{Γ_j} is a scaled version of the non-coherent cost metric in (13) defined as

$$\epsilon_{\Gamma_j} = 20 \log_{10} \sqrt{\frac{1}{K} \mathbf{Y}^H \mathbf{Y} - 2 |\mathbf{Y}^H \mathbf{S}_{\Gamma_j}| + \mathbf{S}_{\Gamma_j}^H \mathbf{S}_{\Gamma_j}} \quad (11)$$

for K data samples. Additional model discrimination tests are applied to the best-fit model estimates to determine the final feature shape classification decision.

3) *RCS Consistency*: The RCS consistency check proposed in [12] verifies that the estimated feature size corresponds to the observed scattering intensity. We define the RCS consistency test as

$$\hat{C} = \arg \left\{ \left| 20 \log_{10} \left(\frac{A_{\text{cal}}(\hat{L}, \hat{H}, \hat{r}, \Gamma_j)}{\hat{A}(\Gamma_j)} \right) \right| < \tau_{\text{RCS}} \right\} \quad (12)$$

where $\hat{A}(\Gamma_j)$ is the estimated model amplitude corresponding to the scalar A in the M_Γ terms of Table I, $A_{\text{cal}}(\hat{L}, \hat{H}, \hat{r}, \Gamma_j)$ is the calibration amplitude factor defined in Table I, evaluated using the estimated object sizes, and \hat{C} is a list of feature types Γ_j satisfying the above inequality.

4) *Object Size Test*: We also check that the estimated object sizes are reasonable compared to the scene size—for example, the results in Section V check for object sizes between 0.01m and 1m.

5) *Combined Model Discrimination Tests*: We implement the three discriminators of model fit, RCS, and size to choose the best model for the data. In practice, multiple or no shapes may pass all of the discrimination tests, so we combine the discrimination tests as follows. In the case that one or more models pass all three discrimination tests, we choose the model with the lowest cost given by (11). In the case when no candidate models pass all three discrimination tests, we choose the lowest cost model that passes the object size test. If no models pass the size test, then we choose the lowest cost model.

E. Feature Estimation with CLEAN

The CLEAN [9] strategy iteratively estimates and removes signals from the data set, starting with the largest energy contributor to the observations. At each iteration i , we estimate the i th shape model's parameters as

$$\hat{\Theta}_i = \arg \min_{\Theta_i} \{ \mathbf{Y}^{(i)H} \mathbf{Y}^{(i)} - 2 \text{abs} \{ \mathbf{Y}^{(i)H} \mathbf{S}_i(k, \Lambda; \Theta_i, \Gamma_i) \} + \mathbf{S}_i^H(k, \Lambda; \Theta_i, \Gamma_i) \mathbf{S}_i(k, \Lambda; \Theta_i, \Gamma_i) \}, \quad (13)$$

for each candidate type Γ_i , choose the best match according to the shape classification tests, and subtract the corresponding signal estimate from the data to obtain a new set of observations

$$\mathbf{Y}^{(i+1)} = \mathbf{Y}^{(i)} - \hat{\mathbf{S}}_i(\Lambda; \hat{\Theta}_i, \hat{\Gamma}_i), \quad (14)$$

repeating the process until a desired number of signals or a desired level of energy is modeled. For point scatterers, the SAR image provides both a location and amplitude estimate for the largest contributing point at each iteration. For the canonical shape models of interest, not all parameters are estimable from the image, but the sparse 3D images help to initialize the search region in high-dimensional parameter space. Note that in (13) we have approximated the LS solution with a non-coherent cost function that contains fewer local minima, allowing for less accurate initial estimates [11]. Nonetheless, we constrain the optimization of (13) such that the location and orientation estimates are near the initialization points and

the size and amplitude parameters are positive-valued scalars. We fit all candidate models with the bounce type determined from the polarimetric scattering response. Then, we follow the feature discrimination scheme described in Section III-D5. We subtract the selected scatterer model phase history from the observations and repeat the process, from image formation to parameter estimation, until a desired number of scatterers or a desired energy level is modeled. A summary of the entire feature extraction process is given in the next section.

We note that estimation errors may result in high-energy residual scattering in the image domain, in which case the CLEAN algorithm will attempt to fit multiple canonical shapes to the same region. However, since the scatterers considered are well-separated and nearly uncorrelated, we do not re-select voxels in the image for which we have already estimated a response. This modification of CLEAN is computationally practical, though estimation errors are still present in the phase history. The impact of the errors on estimating subsequent high-amplitude scattering signals is small, but low-amplitude scatterers may be difficult to estimate if the error terms become large relative to the scatterer of interest.

IV. FEATURE EXTRACTION ALGORITHM SUMMARY

Given phase history collected on (or interpolated to) a Cartesian grid,

- 1) Compute composite ℓ_1 -regularized LS image \hat{s}_c .
- 2) Segment largest-energy region in image.
- 3) Classify image segment polarization response as *odd* or *even* bounce scatterer type.
- 4) Initialize parameters for each canonical model whose bounce type corresponds to that estimated in the region.
- 5) For each candidate model, refine parameter estimates by numerically optimizing non-coherent cost function between observations and candidate model.
- 6) For all models within τ_{fit} of the best-fit model, compute RCS consistency check in (12).
- 7) Check that size estimates are within acceptable bounds.
- 8) Choose estimated model to be best-fit model that passes the size and RCS consistency checks according to the hierarchy given in Section III-D5.
- 9) Subtract estimated model from observed phase history.

Repeat Steps 1-9 until meeting a user-specified, maximum number of iterations or desired level of modeled energy.

V. NUMERICAL RESULTS

We apply the feature extraction algorithm of Section III to simulated bistatic SAR data of a scene comprised of seven canonical shapes. The scene is depicted in Figure 1. We simulate four polarization channels of SAR data using the model signals in Table I. In this experiment, the receiver traverses the arbitrary “squiggle path” shown in Figure 2(a), and the transmitter is fixed at $(\phi_t, \theta_t) = (0^\circ, 30^\circ)$, near the center of the receiver path.

Since the SAR phase history data lies on a sparse aperture in three-dimensions, the corresponding Fourier image (Figure 2(b)) contains high sidelobes and aliasing that make it

difficult to discern the scatterers in the image. However, the sparse image shown in Figure 3 contains distinct scattering regions corresponding to the canonical shapes in the scene. The modified Peak Region Segmentation algorithm locates seven scattering regions of interest, shown in Figure 4. For each image segment in Figure 4, we estimate the polarization bounce types from (9). The estimated bounce types are shown in Figure 5 and agree with the true shape types. Using the image segmentation and polarization bounce results, we obtain initial parameter estimates for the candidate model types in each region. We then fit canonical shape models to the phase history data using the CLEAN method.

Table II lists the estimated size and amplitude parameters for each candidate shape along with the results of the model discrimination tests described in Section III-D. Shapes selected by combining the model discrimination tests are highlighted in green, indicating correct classification. The estimated parameters for the selected shapes are listed in Table III, along with the true feature types and parameters. The final shape estimates are depicted by iconic representations in Figure 6, in which the icon represents the estimated feature type, location, orientation, and size. In the example shown, all seven shapes are correctly classified. The parameter estimates for each shape converge near the true parameter values, except for the dihedral height in image segment #1, which is estimated to be more than twice the true height of the dihedral. The estimated dihedral does fail the RCS consistency test, which correctly indicates a poor amplitude, or as in this case, a poor size estimate due to convergence to a local minima. However, Figure 6 shows the estimated scene geometry is in general a very good match to the true scene in Figure 1.

VI. CONCLUSION

We have presented an algorithm for extraction of 3D geometrical features from sparse, non-linear SAR apertures. The feature estimation approach is an extension of the CLEAN algorithm that iterates estimation and removal of canonical shape signals. We use regularization to form sparse 3D images that allow us to discern scatterers in the scene and initialize 3D canonical shape model estimates. We have shown example results for the proposed feature extraction algorithm for an arbitrary bistatic SAR aperture; however, the algorithm may also be applied to monostatic apertures (see [11] for examples). Future work will apply the proposed feature extraction algorithm to SAR data of vehicle targets.

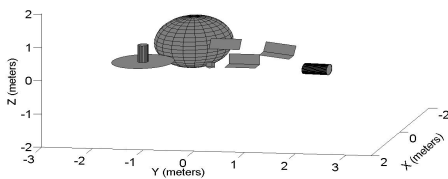


Fig. 1. Scene comprised of seven canonical shape scatterers.

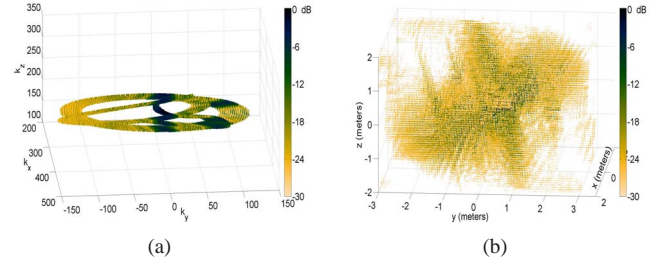


Fig. 2. (a) Composite phase history for a receiver “squiggle path” and a fixed transmitter at $(\phi_t, \theta_t) = (0^\circ, 30^\circ)$ near the center of the receiver aperture and (b) the corresponding HH polarization Fourier image.

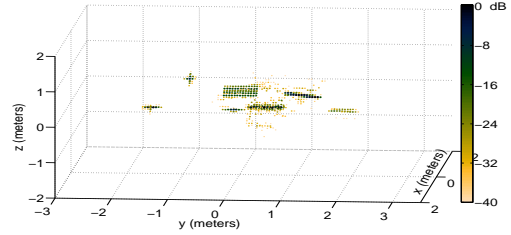


Fig. 3. Composite sparse image for sparsity constraint $\lambda = 25$.

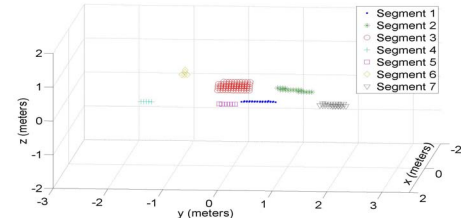


Fig. 4. Image regions detected in Figure 3 by the image segmentation algorithm described in Section III-B.

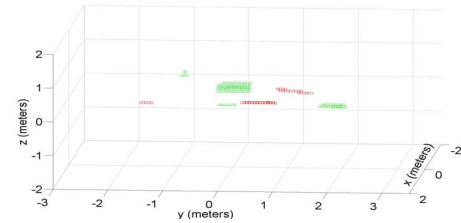


Fig. 5. Bounce types estimated from polarimetric responses of segmented image regions shown in Figure 4. Red squares represent even-bounce voxels and green triangles indicate odd-bounce voxels.

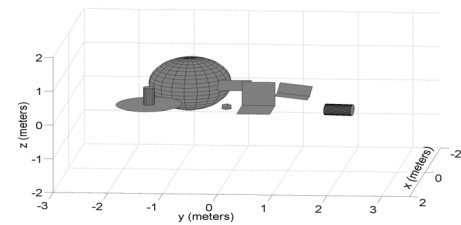


Fig. 6. Iconic representations of the estimated features.

Image Segment #	Candidate Shape Type	Estimated Size and Amplitude					Discrimination Test Values		Does Shape Pass Tests?		
		\hat{L}	\hat{H}	\hat{r}	\hat{A}_{cal}	\hat{A}	$20 \log_{10}(\frac{\hat{A}_{cal}}{\hat{A}})$	NC Cost dB	Fit ($\tau_{fit} = 5$)	Size [0.01, 1]m	RCS ($\tau_{RCS} = 5$)
1	dihedral	0.604	0.694	—	0.839	0.364	7.244	-68.808	yes	yes	no
1	top-hat	—	0.000	0.000	0.000	0.011	— ∞	-65.488	yes	no	no
2	dihedral	0.600	0.301	—	0.361	0.360	0.036	-68.599	yes	yes	yes
2	top-hat	—	0.820	0.253	0.980	0.246	12.007	-65.709	yes	yes	no
3	plate	0.600	0.300	—	0.180	0.180	0.002	-68.859	yes	yes	yes
3	cylinder	0.700	—	0.071	0.186	0.447	-7.596	-66.382	yes	yes	no
3	trihedral	—	0.467	—	0.756	0.117	16.245	-66.417	yes	yes	no
3	sphere	—	—	0.346	0.346	0.453	-2.325	-65.599	yes	yes	yes
4	dihedral	0.026	0.532	—	0.027	0.047	-4.684	-69.024	yes	yes	yes
4	top-hat	—	0.499	0.100	0.376	0.376	-0.005	-69.235	yes	yes	yes
5	plate	0.172	0.000	—	0.000	0.020	— ∞	-67.803	yes	no	no
5	cylinder	0.171	—	0.103	0.055	0.180	-10.293	-68.410	yes	yes	no
5	trihedral	—	0.120	—	0.050	0.050	0.054	-68.351	yes	yes	yes
5	sphere	—	—	0.521	0.521	0.617	-1.459	-66.691	yes	yes	yes
6	plate	0.117	0.037	—	0.004	0.013	-9.558	-67.050	yes	yes	no
6	cylinder	0.122	—	0.135	0.045	0.104	-7.367	-67.041	yes	yes	no
6	trihedral	—	0.088	—	0.027	0.042	-3.823	-66.933	yes	yes	yes
6	sphere	—	—	0.750	0.750	0.750	-0.002	-68.490	yes	yes	yes
7	plate	0.501	0.020	—	0.010	0.024	-7.581	-67.598	yes	yes	no
7	cylinder	0.500	—	0.151	0.195	0.194	0.039	-67.618	yes	yes	yes
7	trihedral	—	0.033	—	0.004	0.008	-6.477	-65.699	yes	yes	no
7	sphere	—	—	0.000	0.000	0.147	— ∞	-65.656	yes	no	no

TABLE II

ESTIMATED SHAPE SIZES AND AMPLITUDES AND MODEL DISCRIMINATION RESULTS. HIGHLIGHTED ROWS INDICATE THE SHAPE SELECTED FOR EACH REGION USING THE MODEL FIT, OBJECT SIZE, AND RCS CONSISTENCY DISCRIMINATION TESTS.

Segment #	Estimate Type	Detected Shape	Parameters									
			x	y	z	$\tilde{\gamma}$	$\tilde{\theta}$	$\tilde{\phi}$	L	H	r	A
1	Truth	dihedral	0.25	0.5	0	0	0	0	0.6	0.3	—	0.36
1	Final	dihedral	0.250	0.499	0.000	0.066	-0.317	0.033	0.604	0.694	—	0.364
2	Truth	dihedral	0	1.1	0.25	-10	0	0	0.6	0.3	—	0.36
2	Final	dihedral	0.000	1.100	0.250	-10.004	0.000	-0.002	0.600	0.301	—	0.360
3	Truth	plate	-0.1	0	0.3	0	-30	0	0.6	0.3	—	0.18
3	Final	plate	-0.100	0.000	0.300	0.133	-29.999	-0.000	0.600	0.300	—	0.180
4	Truth	top-hat	0.25	-1.5	0	0	0	0	—	0.5	0.1	0.38
4	Final	top-hat	0.250	-1.500	-0.000	-0.005	-0.002	0.000	—	0.499	0.100	0.376
5	Truth	trihedral	0.75	0	0.1	0	0	0	—	0.12	—	0.05
5	Final	trihedral	0.748	0.000	0.106	-1.222	-0.375	-0.768	—	0.120	—	0.050
6	Truth	sphere	-1.5	-1	0	—	—	—	—	—	0.75	0.75
6	Final	sphere	-1.500	-1.000	0.000	—	—	—	—	—	0.750	0.750
7	Truth	cylinder	0.5	2	0	0	0	-5	0.5	—	0.15	0.19
7	Final	cylinder	0.499	2.000	-0.001	0.001	0.912	-4.999	0.500	—	0.151	0.194

TABLE III

CANONICAL SHAPE PARAMETER TRUTH AND FINAL PARAMETER ESTIMATES FOR THE DETECTED SHAPES HIGHLIGHTED IN TABLE II.

REFERENCES

- [1] M. Cetin and W. C. Karl, "Feature-enhanced synthetic aperture radar image formation based on nonquadratic regularization," *IEEE Transactions on Image Processing*, vol. 10, no. 4, pp. 623–631, April 2001.
- [2] T. Kragh and A. Kharbouch, "Monotonic iterative algorithms for SAR image restoration," *Image Processing, 2006 IEEE International Conference on*, pp. 645–648, Oct. 2006.
- [3] C. D. Austin and R. L. Moses, "Wide-angle sparse 3D synthetic aperture radar imaging for nonlinear flight paths," in *IEEE National Aerospace and Electronics Conference (NAECON) 2008*, July 16–18 2008.
- [4] J. A. Jackson, B. D. Rigling, and R. L. Moses, "Parametric scattering models for bistatic synthetic aperture radar," *2008 IEEE Radar Conference*, pp. 1–5, May 26–30, 2008, Rome, Italy.
- [5] —, "Canonical scattering feature models for 3D and bistatic SAR," *IEEE Transactions on Aerospace and Electronic Systems*, in press.
- [6] J. B. Keller, "Geometrical theory of diffraction," *J. Opt. Soc. Amer.*, pp. 116–130, Jan 1962.
- [7] M. A. Koets and R. L. Moses, "Image domain feature extraction from synthetic aperture imagery," in *IEEE International Conference on Acoustics, Speech, and Signal Processing*, vol. 4, March 1999, pp. 2319–2322.
- [8] J. A. Jackson and R. L. Moses, "Feature extraction algorithm for 3D scene modeling and visualization using monostatic SAR," in *Algorithms for Synthetic Aperture Radar Imagery XIII, Proceedings of SPIE*, E. G. Zelnio and F. D. Garber, Eds., vol. 6237, 2006.
- [9] J. A. Hogbom, "Aperture synthesis with a non-regular distribution of interferometer baselines," *Astronomy and Astrophysics Supplement Series (0365-0138)*, vol. 15, no. 3, pp. 417–426, 1974.
- [10] J. Stach and E. LeBaron, "Enhanced image editing by peak region segmentation," *Antenna Measurement Techniques Association; 18th Annual Meeting and Symposium*, pp. 303–307, Sept. 30 - Oct. 3 Seattle, Washington, 1996.
- [11] J. A. Jackson, *Three-Dimensional Feature Models for Synthetic Aperture Radar and Experiments in Feature Extraction*. The Ohio State University: Ph.D. Dissertation, 2009.
- [12] J. A. Jackson and R. L. Moses, "Identifiability of 3D attributed scattering features from sparse nonlinear apertures," in *Algorithms for Synthetic Aperture Radar Imagery XIV, Proceedings of SPIE*, E. G. Zelnio and F. D. Garber, Eds., vol. 6568, 2007.